Electronic supplementary information for

Imaging atomic motion of light elements in 2D materials with 30 kV electron microscopy

Sytze de Graaf[1], Majid Ahmadi[1], Ivan Lazić[2], Eric G.T. Bosch[2], Bart J. Kooi[1*]*

[1]Zernike Institute for Advanced Materials, University of Groningen, Nijenborgh 4, 9747 AG Groningen, The Netherlands.

[2]Thermo Fisher Scientific, Achtseweg Noord 5, 5651 GG Eindhoven, The Netherlands.

[*]sytze.de.graaf@rug.nl, b.j.kooi@rug.nl.

1. Sample preparation of 2D WS_2 for scanning transmission electron microscopy analysis

Monolayer flakes of WS_2 were either transferred to, or directly grown on, Si/SiO_2 (300 nm) substrates by, respectively, exfoliating bulk crystals (HQ Graphene) with the scotch tape method for Fig. 1a-d and Fig. 2-4, or using chemical vapor deposition (CVD) for Fig. 1e-h. The monolayer flakes were identified using optical microscopy (Fig. S1a) and transferred to R 1.2/1.3 carbon Quantifoil TEM grids with a poymer free method (Fig. S1b-d).

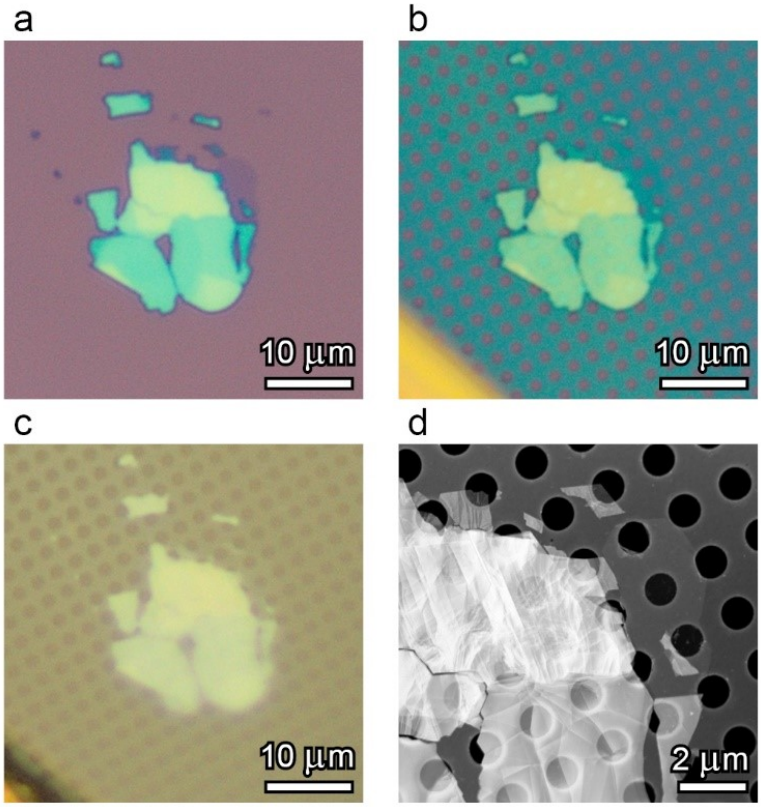

Figure S1. Microscope images of the exfoliated WS_2 flake taken after different steps of the transfer method. (a) The exfoliated WS_2 flake on Si/SiO_2 (300 nm) substrate, with a monolayer part in the top right (dark contrast). (b) Perforated carbon support grid of the TEM grid is attached to the flake after the isopropanol has evaporated. Bottom left shows a part of the gold grid. (c) TEM grid with WS_2 flake is detached from the Si/SiO_2 substrate after etching in 1M KOH. (d) Overview ADF-STEM image of the WS_2 flake. Weak contrast of the monolayer part is visible at the upper right part of the flake.

First, the TEM grid is carefully put on top of the monolayer WS_2 with the carbon support film facing the flake. One droplet of isopropanol is placed on the TEM grid, which directly wets both the carbon film and the SiO_2 substrate to form a liquid interface between them. The flexible TEM grid is pulled towards the flake and the substrate upon evaporation of the isopropanol, which results in strong adhesion of the TEM grid to the WS_2 flake and substrate (Fig. S1b). The entire stack (substrate/flake/TEM grid) is then immersed in a 1M KOH solution at room temperature to etch away the SiO_2, for as long as necessary to detach the TEM grid (usually 5-15 minutes). Then the TEM grid is carefully extracted from the solution with self-closing tweezers, which are then dried together (as otherwise the TEM grid sticks to the tweezer upon opening due to the liquid capillary) for 5-10 minutes in an atmospheric furnace at 70-80 °C. The dried TEM grid is floated on deionized water (with carbon support film facing up) for 15-30 minutes to rinse off precipitated KOH crystals. Note that the drying step prior to rinsing in water is crucial, as otherwise the carbon film is found to very easily detach from the gold grid when floating the grid on water. Finally, the grid is scooped with filter paper and dried for 5-10 minutes in an atmospheric furnace at 70-80 °C (Fig. S1c).

2. Scanning transmission electron microscopy experimental conditions and image processing

Here we have used a state-of-the-art 30-300 kV Thermo Fisher Themis Z scanning transmission electron microscope. The microscope is equipped with a high coherence, high brightness field-emission electron gun (X-FEG), electron monochromator, probe C_S corrector (S-CORR), image C_S corrector (CETCOR) and a segmented DF4 detector for iDPC-STEM imaging.

The microscope was stabilized over the weekend after changing the high-tension to 30 kV. Then the aberrations up to the 5^{th} order were minimized with the probe corrector software to the measured values shown in Table S1. During the experiments, the first and second order aberrations were minimized using the OptiSTEM software, which employs a contrast optimization algorithm of atomic resolution ADF-STEM images. Finetuning of defocus (C1), first order astigmatism (A1) and coma (B2) was done manually.

These low aberration values produce a phase front with a phase difference less than $\pi/2$ up to 50 mrad, such that an optimal small electron probe can be obtained with a convergence semi-angle up to this value. In our case, however, the largest suitable limiting aperture was 33 mrad, restricting the fundamental achievable resolution to 1.06 Å, which we closely reached in experiment. Because we do observe the WS_2 (20-20) planes (1.36 Å) and not the next following (12-30) planes (1.03 Å). Resolution below 1 Å can be obtained with larger better matching limiting apertures such that the probe corrector is used to its full potential.

Table S1. A list of measured aberration values and confidence levels after tuning the probe C_S corrector at 30 keV.

Aberration	**Value**	**95% confidence**
WD	300 μrad	N/A
C1	3 nm	1 nm
A1	2 nm	1 nm
A2	13 nm	43 nm
B2	28 nm	42 nm
C3	-540 nm	1 μm
A3	210 nm	400 nm
S3	220 nm	330 nm
A4	3.4 μm	2.7 μm
D4	2.6 μm	1.8 μm
B4	4.2 μm	3.4 μm
C5	240 μm	320 μm
A5	240 μm	47 μm
S5	100 μm	74 μm

At these low electron beam energies, the probe broadening due to chromatic aberrations has substantial impact. For instance, atomic resolution could hardly be achieved without reducing the energy spread of the electron source. Hence, the energy spread was reduced by employing the monochromator, which was excited to a value of 0.35, after which the microscope was stabilized overnight. With the circular energy selecting apertures of 0.5 and 1.0 μm that we employed, the maximum available probe current was about 3 pA and 8 pA, respectively. As the

microscope is not equipped with a spectrometer we could not measure the energy spread, thus we estimate (based on the size of the dispersed beam and aperture size) the energy spread as ~0.2-0.3 eV. The collection angles of the segmented DF4 detector and ADF detector were 9-36 mrad and 39-200 mrad, respectively.

For Fig. 1 in the main article an image of 512x512 pixels was acquired with 7.5 pA probe current, 40 μs/pixel dwell time and a step size of 15.92 pm. For Figs. 2-4 in the main article, a 200-frame movie of 512x512 pixels was acquired with 2.5 pA probe current, 50 μs/pixel dwell time and a step size of 22.52 pm. Thus, the electron doses were about 7.4×10^4 $e^-/Å^2$ and 1.5×10^4 $e^-/Å^2$ for Fig. 1 and Figs. 2-4, respectively. Despite the larger energy spread, due to using a larger energy selecting aperture, the image quality of Fig. 1 is predominantly improved as a result of the more than 5 times as high electron dose.

Specimen drift is another critical component that should be minimized in order to be able to continuously capture the same field of view for prolonged acquisition times. The original images, from which Figs. 2-4 in the main article were extracted, have a field of view of about 11 x 11 nm^2, and were acquired with a frame rate of 14.0 seconds per frame, yielding a total acquisition time of 2800 seconds, or about 45 minutes. In this case the specimen drifted 2.5 nm within the first 50 frames yielding a drift rate of 0.22 nm/min. Thereafter, in the remaining 150 frames, the specimen was virtually stable with a total drift distance of 1 nm (drift rate of 0.03 nm/min). This is possible by the active vibrational damping system of the microscope column, ultra-stable room temperature (maximal deviation of 0.2 °C/24 hours), and the use of a piezo controlled stage.

The ADF- and iDPC-STEM images were bandpass filtered with Fiji[1,2] using the 'FFT Bandpass Filter' with a low-pass filter of 3 pixels, and a high-pass filter of 10 pixels, a standard operation in 2D materials research. The DPC-STEM images were bandpass filtered in MATLAB with a

Gaussian low-pass filter with standard deviation of 3.0 nm^{-1}, and a Gaussian high-pass filter with a standard deviation of 1.0 nm^{-1}. We explicitly note that low-pass filtering can be safely applied to any STEM imaging technique, as only noise and no information is present at frequencies beyond twice the convergence semi-angle (see below for detailed explanation). We observe that particularly the quality of ADF-STEM images improves by low-pass filtering, as a substantial amount of high-frequency noise is present that otherwise totally obscures the light elements in the raw images. On the other hand, high-pass filtering is beneficial for iDPC-STEM images, because iDPC-STEM has strong contrast transfer at low-frequency information, which is mainly surface adsorbates and carbon contamination in this case. We refer the reader to our previous work for a comparison of filtering on ADF- and iDPC-STEM images[3]. Furthermore, the DPC-STEM images were deliberately strongly low-pass filtered (removing not only high-frequency noise but also high-frequency information) to enhance visibility of defect features.

The separate frames of Fig. 2-4 are compiled to a movie and are attached as Movie S1, Movie S2 and Movie S3, respectively. There simultaneously acquired iDPC-STEM, DPC-STEM and ADF-STEM images are shown, with the effective elapsed time (for the whole field of view) indicated in the top left corner.

3. Comparison of experimental and simulated iDPC-STEM and ADF-STEM images of 2D WS_2

In Fig. S2 we compare the experimental images from Fig. 1 of the main article with multislice image simulations[4]. For the simulations we have used the experimental optical settings, assume an ideal aberration free probe, and account for thermal vibrations of the sample via a Gaussian distribution with a 5 pm standard deviation. We have introduced randomly distributed sulfur vacancies in the top and bottom sulfur layer, yielding several V_S and V_{2S} in the 2D WS_2.

The simulated (Fig. S2a) and experimental (Fig. S2c,d) iDPC-STEM images match strikingly well. Both show similar sensitivity for the sulfur atoms and their vacancies, which can be easily and robustly visually identified based on their relative intensities. In fact, there is also a good quantitative match as plotted in Fig. S2g. We note however, that the simulations reveal that four detector segments are not completely accurate in the electrostatic potential imaging, considering that the S_2 column has higher intensity than the heavier W atom. In the next section we discuss this observation in more detail.

On the other hand, the simulated ADF-STEM images (Fig. S2b) predict the sulfur atoms and also the vacancies to be visible and distinguishable by visual inspection. However, in experiment (Fig. S2e,f) we find the ADF-STEM images to be rather noisy (even after low-pass filtering) with limited robustness towards the light sulfur atoms such that the vacancies can hardly be identified. Also, the quantitative comparison in the intensity line profile plot (Fig. S2h) demonstrate that only the heavy W atoms are robustly imaged, but the S atoms have reduced intensity, not allowing one to distinguish the S atoms and vacancies visually.

Hence, this comparison emphasizes that iDPC-STEM is more sensitive and more dose-efficient compared to ADF-STEM. Clearly, this is expected based on the detector geometry: the ADF detector collects substantially less electrons than the DF4 detector. However, additionally, the

high signal-to-noise ratio is an inherent property of iDPC-STEM due to the integration operation.

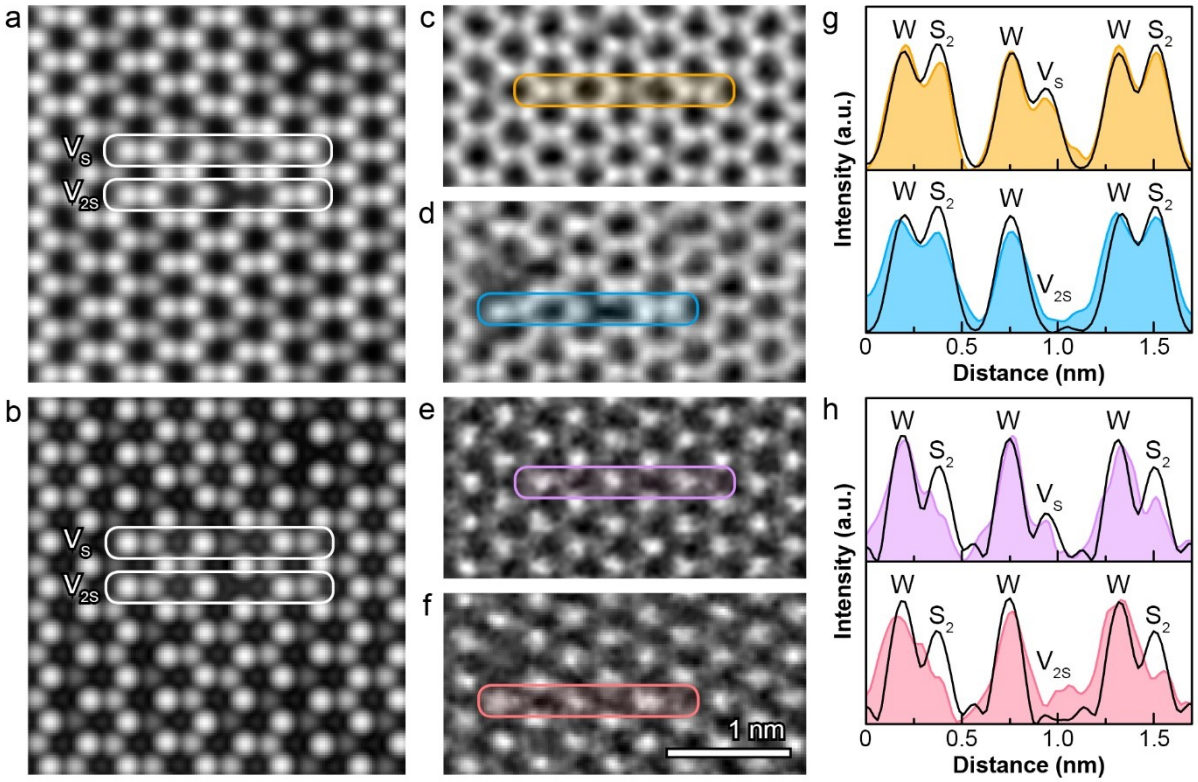

Figure S2. Comparison of simulated and experimental images (from Fig.1 of the main article) of point defects in 2D WS_2. Intensity line profiles containing sulfur vacancies and sulfur divacancies are extracted from the simulated iDPC-STEM (a) and ADF-STEM images (b) as indicated by the outlined areas, and plotted as black lines in (g) and (h), respectively. Identical defects are also extracted from the experimental iDPC-STEM (c,d) and ADF-STEM (e,f) images, and plotted in (g) and (h) with the same color coding as outlined in (c-f).

4. Robust atomic electrostatic potential imaging of light elements in 2D WS_2

The capability of robust imaging of misaligned materials is particularly valuable in the case of transition metal dichalcogenides (TMDs) with the 2H symmetry, because in that case the two chalcogen atoms in a monolayer overlap in projection when it is perfectly aligned along the (0001) crystal zone axis, boosting their atomic resolution signal. However, in practice the 2D TMDs can be easily misaligned with respect to the optical axis of the electron beam.

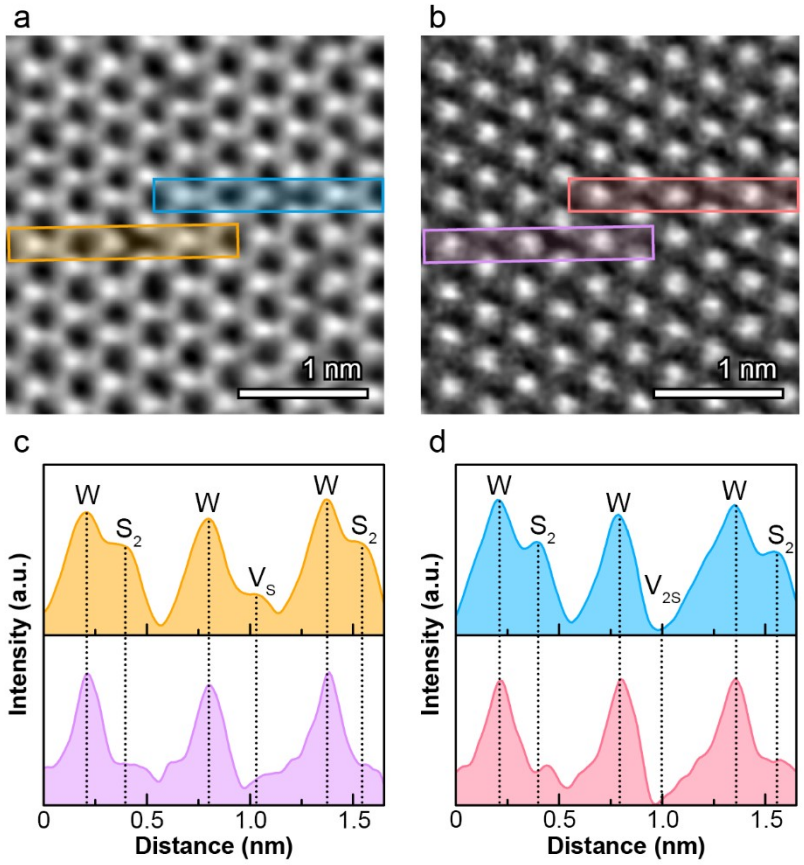

Figure S3. Images of a monolayer 2H WS_2 with V_S and V_{2S} were acquired from a region that was misaligned by a few degrees from the (0001) zone axis. It shows how iDPC-STEM (a) robustly images the sulfur vacancies with single sulfur atom sensitivity as opposed to ADF-STEM in (b). Line profiles from V_S and V_{2S} are shown in (c,d), from the rectangular regions marked in (a,b).

Slight bending/buckling of the suspended 2D material flake on the TEM grid can be expected, e.g. as a result of the strong capillary forces of the liquid used during TEM sample preparation that create residual stress upon drying. Hence, it is a challenging task to well-align the 2D material locally, since the alignment fluctuates on a lateral scale of just tens of nanometers. In Fig. S3 we show the simultaneously acquired iDPC-STEM and ADF-STEM image of a (few degrees) misaligned monolayer 2H WS_2. These results demonstrate that it is still possible to properly detect and distinguish single and double sulfur vacancies (V_S and V_{2S}) with iDPC-STEM, but not with ADF-STEM, which nearly lost all its sensitivity towards sulfur.

5. Simulated contrast and accuracy of atomic electrostatic potential imaging of 2D WS_2 with iDPC-STEM

The finite resolution of the electron microscope poses a fundamental limit on the contrast between W and S_2 in the case of a 2H WS_2 monolayer. Specifically, in the case of ADF-STEM and iDPC-STEM, information is only transferred up to a wavevector (i.e., reciprocal length or frequency) that is twice the length of the largest wavevector present in the electron probe. In our case, with a convergence semi-angle of 33 mrad and electron wavelength of about 7 pm, the largest wavevector present in the electron probe is 4.7 nm^{-1}. Which corresponds to maximum information transfer at 9.4 nm^{-1}, or 1.06 Å.

In Fig. S4 we have simulated the atomic potential of a 2H WS_2 monolayer using the multislice approach with the Dr. Probe software[5]. We neglect atomic thermal vibrations and we assume an aberration free electron probe, to demonstrate the effects of finite resolution and reduced accuracy of atomic potential imaging with iDPC-STEM. In Fig. S4a the simulated atomic potentials of a 2H WS_2 monolayer are shown, which we use as the 'true ground state' for further comparison. The bandwidth limited atomic potentials of WS_2 are shown in Fig. S4b. The corresponding line profiles in Fig. S4e,f demonstrate how the contrast between W and S_2 reduces from a relative intensity of 1.8 to 1.25 by just imposing the fundamental information transfer limit.

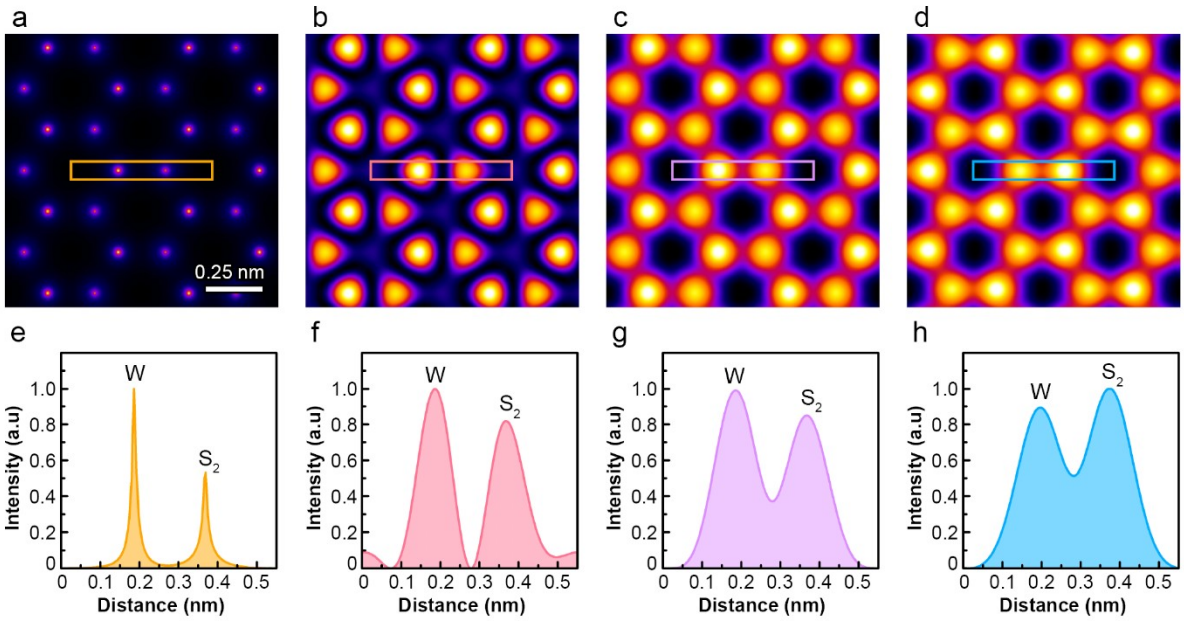

Figure S4. Simulated images of atomic electrostatic potentials of 2H WS_2 monolayer using the multislice approach. (a) The 'true ground state' atomic electrostatic potentials, which are the input for multislice simulations. (b) The atomic electrostatic potentials from (a) are bandwidth limited to the maximum transferrable wavevector to obtain the highest possible resolution image. (c) A simulated iCOM-STEM image (ideal version of iDPC-STEM when enough segments are used) based on the atomic electrostatic potentials in (a). (d) A simulated iDPC-STEM image using four detector segments based on the atomic electrostatic potentials in (a). Line profiles of the W and S_2 atomic electrostatic potentials are plotted in (e-h), corresponding to the marked rectangular area in (a-d).

In fact, the contrast between W and S_2 is slightly lower in the case of iCOM-STEM (Fig. S4c,g) and iDPC-STEM (Fig. S4d,h) than in the bandwidth limited case, because then less high frequency information transfer occurs than that assumed in Fig. S4b. The reason is that the contrast transfer functions (CTF) of iCOM-STEM and iDPC-STEM decreases linearly to zero at the maximum wave vector, whereas the (imposed) contrast transfer function for Fig. S4b keeps a value of one up to the maximum wave vector and then in a step becomes zero.

Note that iCOM-STEM can be considered the most ideal case of iDPC-STEM, that can be achieved when enough detector segments are used. It is important to stress here that the object of imaging (unlike in ADF-, (A)BF- or DPC-STEM) is truly the projected atomic electrostatic potential of the sample, rendering iCOM-STEM (without any approximations) a linear imaging technique. The CTF of iCOM-STEM is positive definite (no zero crossings) with full range frequency transfer near the optimal focus. With larger segment detectors, like commonly used in iDPC-STEM, the COM is determined with less precision (although even with only four detector segments rather well). Nevertheless, even in that case, iDPC-STEM is a dominantly linear imaging technique, with well-defined CTF (reflecting the symmetry of the detector used) including almost negligible correction terms[6]. The contribution of these terms become noticeable only far out of focus for thin samples or in general for rather thick samples[7], where part of the sample is always out of focus.

The iDPC-STEM image (Fig. S4d,h) reveals that the intensity of the S_2 peak even exceeds that of W. This is a direct result of using only four detector segments to approximate the COM, but the accuracy can be readily improved by employing more detector segments. In experiment, however, we observe that the heavier W atom are usually equally bright or slightly brighter than the S_2 atoms.

In experiment both the specimen and the electron probe are not perfect i.e. atomic vibrations, chromatic aberration and finite source size always contribute to the image and cannot be excluded. To this end we have simulated atomic vibrations by the frozen phonon method, where each pixel is averaged over 50 randomly selected variants from a set of 200 pre-computed random atomic vibrations. Isotropic atomic Debye-Waller factors of 0.042 $Å^2$ and 0.398 $Å^2$ are used for W and S, respectively[8]. Chromatic aberrations are accounted for by a defocus spread of 10 nm, assuming an energy spread of 0.25 eV and a chromatic aberration of 2.5 mm. A finite electron source size of 60 pm (full-width at half maximum) is accounted for by applying a

Gaussian convolution to the final images. Finally, also the finite electron dose directly affects the visibility of low signals, which we included by introducing Poisson noise to the images. Naturally, in the case of iDPC-STEM images the Poisson noise is first introduced to each of the detector segments and then the iDPC-STEM image computed.

Fig. S5 presents the simulated ADF-STEM and iDPC-STEM images using such imaging conditions, where the electron dose spans three orders of magnitude and are a good representation of the experimental conditions. The general trend is that atomic vibrations have a minimal effect on the signal of sulfur atoms, but that chromatic aberration and finite probe size lead to broadening of W, S_2 and S and also increase the background signal. A consequence of the latter is that low signals can be obscured and that resolution is lost particularly when combined with lower electron doses of 1×10^3 e/Å^2. This is well visible in the low-dose iDPC-STEM images, which remain of good quality only when chromatic aberration and finite source size are neglected, but loose resolution as soon as they are included.

For a semi-quantitative analysis we have extracted intensity profiles of W-S_2-W-S considering only infinite, 1×10^5 e/Å^2 and 1×10^4 e/Å^2 electron doses, as the latter two represent Fig. 1 and Fig. 2-4 in the main article. These results are plotted in Fig. S6 for ADF-STEM and in Fig. S7 for iDPC-STEM. Single sulfur atoms are not visible in ADF-STEM images (accounting for atomic vibrations, chromatic aberration and finite source size) when the dose is 1×10^5 e/Å^2, and S_2 columns are hardly detected when the dose is further reduced to 1×10^4 e/Å^2. This is not the case for iDPC-STEM where all atoms present remain both detectable and distinguishable in all considered cases.

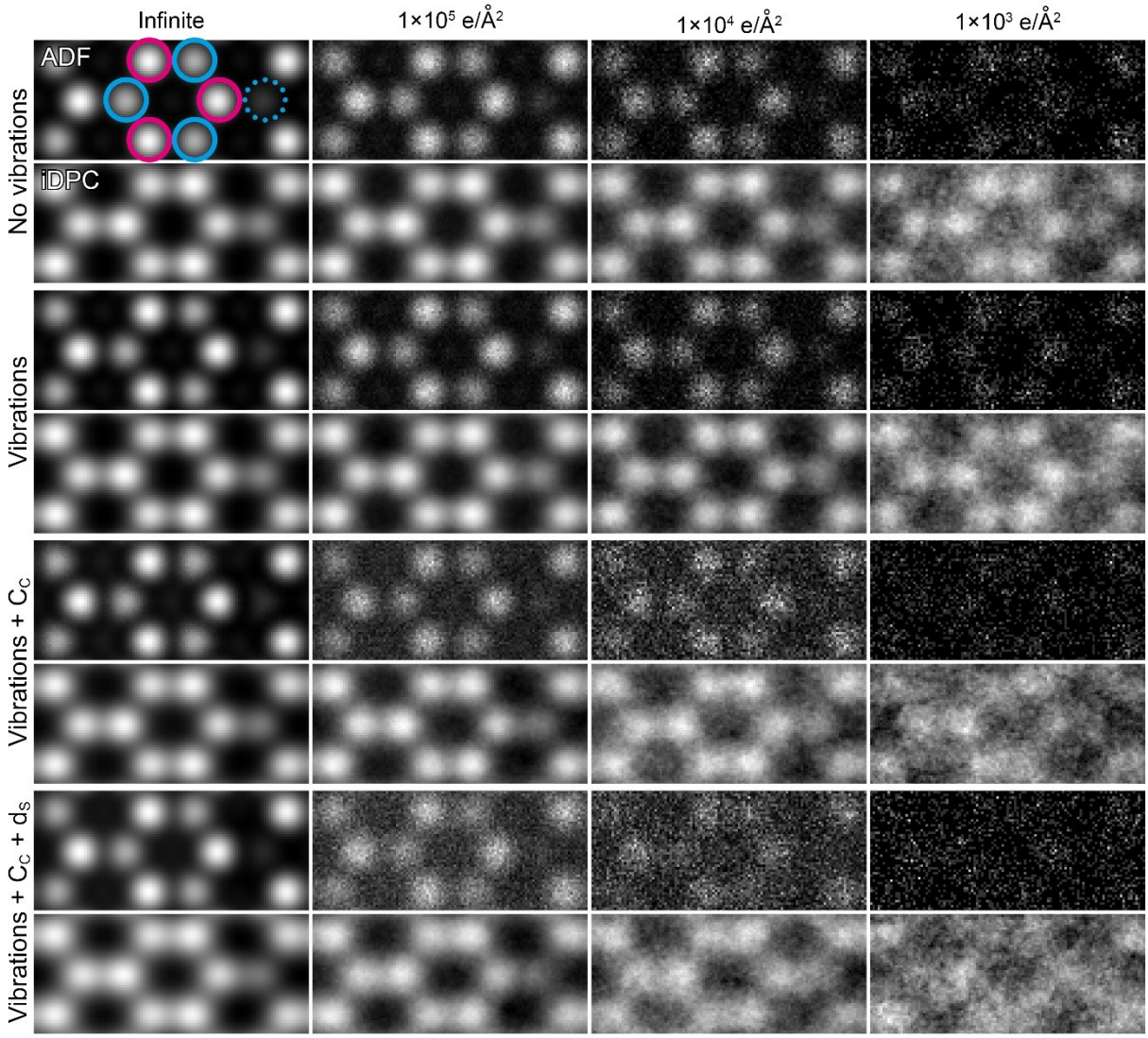

Figure S5. Image simulations of 2D WS_2 including atomic vibrations, chromatic aberration (C_C), finite source size (d_S) and finite electron dose. The top left panel indicates the position of W, S_2 and V_S by solid magenta circles, solid cyan circles and a dotted cyan circle, respectively, and applies to all other panels.

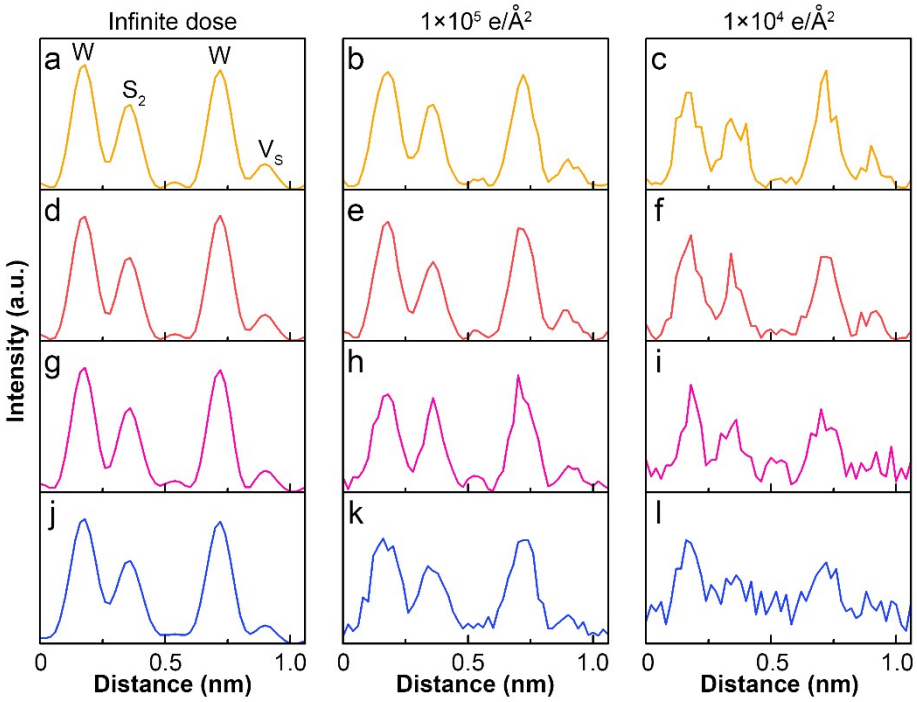

Figure S6. Intensity profiles extracted from simulated ADF-STEM images in Fig. S5, considering various probe broadening effects and also atomic vibrations of the specimen. (a-c) No vibrations and a perfect probe; (d-f) atomic vibrations and a perfect probe; (g-i) atomic vibrations and chromatic aberration; (j-l) atomic vibrations, chromatic aberration and a finite source size.

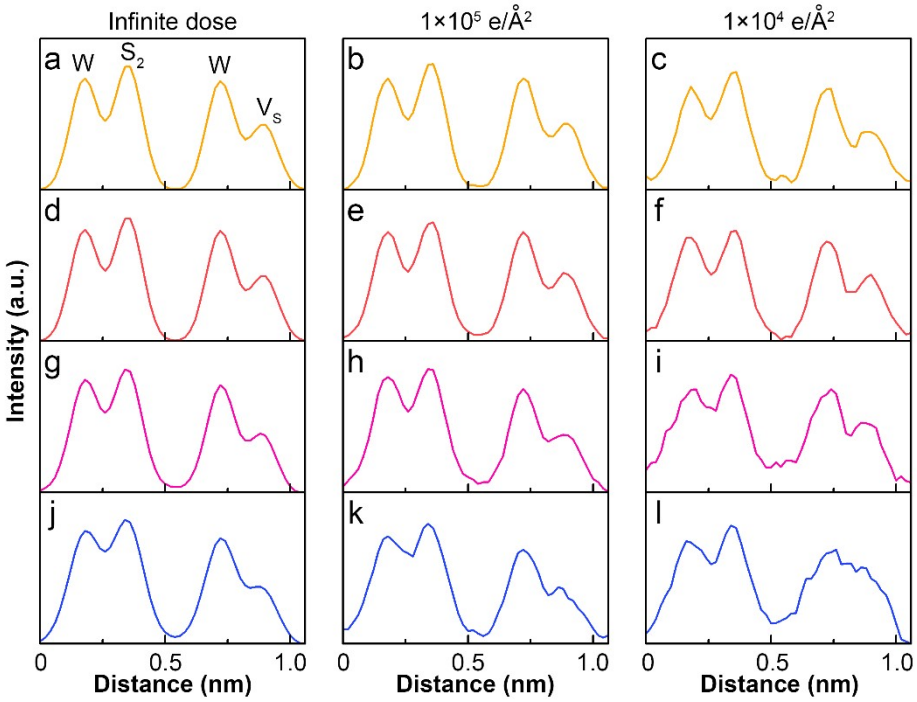

Figure S7. Intensity profiles extracted from simulated iDPC-STEM images in Fig. S5, considering various probe broadening effects and also atomic vibrations of the specimen. (a-c) No vibrations and a perfect probe; (d-f) atomic vibrations and a perfect probe; (g-i) atomic vibrations and chromatic aberration; (j-l) atomic vibrations, chromatic aberration and a finite source size.

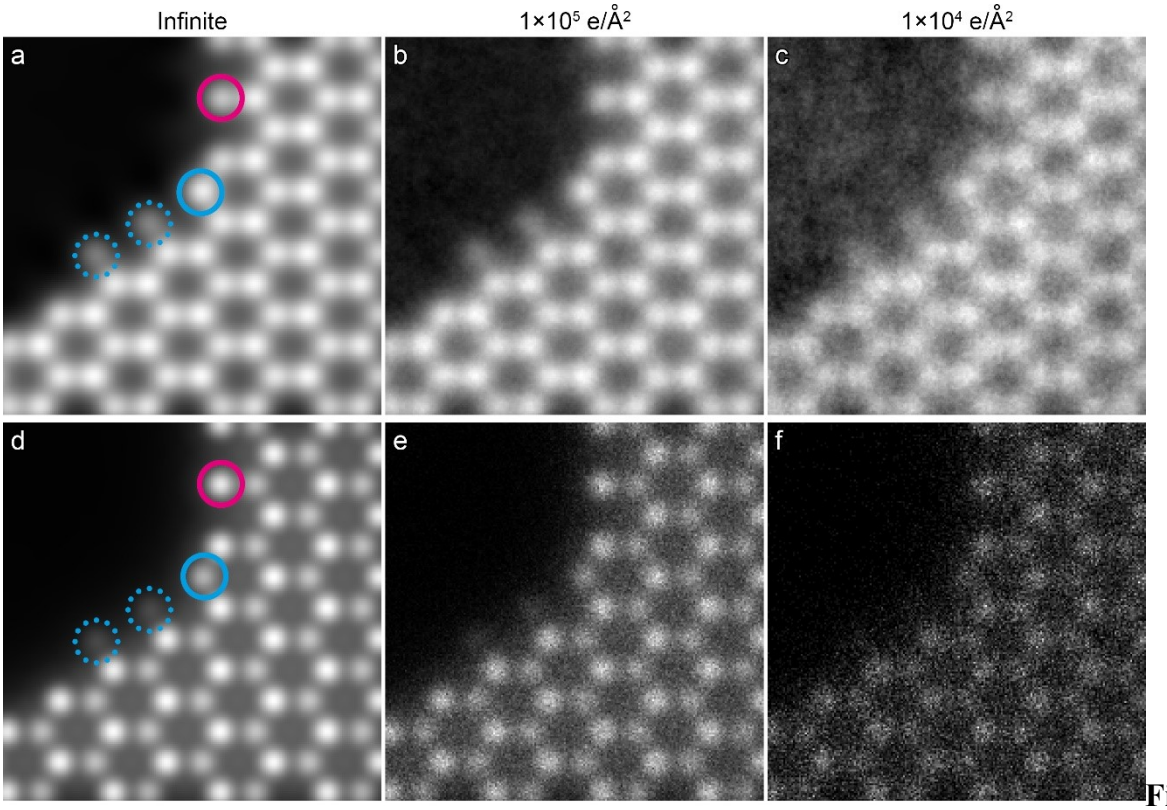

Figure S8. Image simulation of W, S_2 and S atoms at 2D WS_2 edges with (a-c) 30 kV iDPC-STEM and (d-f) 30 kV ADF-STEM with various electron doses. The positions of W, S_2 and S atoms at edges are indicated by a solid magenta circle, solid cyan circle and dotted cyan circles, respectively, and applies to all other panels. Atomic vibrations, chromatic aberrations, finite source size and electron dose have been accounted for as described in section 5.

References

1 J. Schindelin, I. Arganda-Carreras, E. Frise, V. Kaynig, M. Longair, T. Pietzsch, S. Preibisch, C. Rueden, S. Saalfeld, B. Schmid, J.-Y. Tinevez, D. J. White, V. Hartenstein, K. Eliceiri, P. Tomancak and A. Cardona, Fiji: an open-source platform for biological-image analysis, *Nature Methods*, 2012, **9**, 676–682.

2 J. Schindelin, C. T. Rueden, M. C. Hiner and K. W. Eliceiri, The ImageJ ecosystem: An open platform for biomedical image analysis, *Molecular Reproduction and Development*, 2015, **82**, 518–529.

3 S. de Graaf, J. Momand, C. Mitterbauer, S. Lazar and B. J. Kooi, Resolving hydrogen atoms at metal-metal hydride interfaces, *Science Advances*, 2020, **6**, eaay4312.

4 E. G. T. Bosch and I. Lazić, Analysis of HR-STEM theory for thin specimen, *Ultramicroscopy*, 2015, **156**, 59–72.

5 J. Barthel, Dr. Probe: A software for high-resolution STEM image simulation, *Ultramicroscopy*, 2018, **193**, 1–11.

6 I. Lazić and E. G. T. Bosch, in *Advances in Imaging and Electron Physics*, ed. P. W. Hawkes, Elsevier, 2017, vol. 199, pp. 75–184.

7 E. G. T. Bosch and I. Lazić, Analysis of depth-sectioning STEM for thick samples and 3D imaging, *Ultramicroscopy*, 2019, **207**, 112831.

8 R. J. Wu, M. L. Odlyzko and K. A. Mkhoyan, Determining the thickness of atomically thin MoS2 and WS2 in the TEM, *Ultramicroscopy*, 2014, **147**, 8–20.